LAWRENCE
LIVERMORE
NATIONAL
LABORATORY

Radiative shocks produced from spherical cryogenic implosions at the National Ignition Facility

A. Pak, L. Divol, G. Gregori, S. Weber, J. Atherton, R. Bennedetti, D. K. Bradley, D. Callahan, E. Dewald, T. Doeppner, M. J. Edwards, S. Glenn, D. Hicks, N. Izumi, O. Jones, S. F. Khan, J. Kilkenny, J. L. Kline, G. A. Kyrala, J. Lindl, O. L. Landen, S. LePape, T. Ma, A. MacPhee, B. J. MacGowan, A. J. Mackinnon, L. Masse, N. B. Meezan, J. D. Moody, E. Moses, R. E. Olson, J. E. Ralph, H. S. Park, B. A. Remmington, J. S. Ross, R. Tommasini, R. P. J. Town, V. Smalyuk, S. H. Glenzer, W. W. Hsing, H. F. Robey, G. P. Grim, L. J. A Frenje, D. T Casey, M. G. Johnson

December 27, 2012

Disclaimer

This document was prepared as an account of work sponsored by an agency of the United States government. Neither the United States government nor Lawrence Livermore National Security, LLC, nor any of their employees makes any warranty, expressed or implied, or assumes any legal liability or responsibility for the accuracy, completeness, or usefulness of any information, apparatus, product, or process disclosed, or represents that its use would not infringe privately owned rights. Reference herein to any specific commercial product, process, or service by trade name, trademark, manufacturer, or otherwise does not necessarily constitute or imply its endorsement, recommendation, or favoring by the United States government or Lawrence Livermore National Security, LLC. The views and opinions of authors expressed herein do not necessarily state or reflect those of the United States government or Lawrence Livermore National Security, LLC, and shall not be used for advertising or product endorsement purposes.

Radiative shocks produced from spherical cryogenic implosions at the National Ignition Facility

A. Pak,[1] L. Divol,[1] G. Gregori,[2] S. Weber,[1] J. Atherton,[1] R. Bennedetti,[1] D. K. Bradley,[1] D. Callahan,[1] E. Dewald,[1] T. Döpnner,[1] M.J. Edwards,[1] S. Glenn,[1] D. Hicks,[1] N. Izumi,[1] O. S. Jones,[1] S. F. Khan,[1] J.D. Kilkenny,[3] J.L. Kline,[4] G.A. Kyrala,[4] J. Lindl,[1] O. L. Landen,[1] S. Lepape,[1] T. Ma,[1] A. MacPhee,[1] B. J. MacGowan,[1] A. J. MacKinnon,[1] L. Masse,[5] N. B. Meezan,[1] J. D. Moody,[1] E. Moses,[1] R. E. Olson,[6] J. E. Ralph,[1] H.-S. Park,[1] B. A. Remington,[1] J. S. Ross,[1] R. Tommasini,[1] R. P. J. Town,[1] V. Smalyuk,[1] and S. H. Glenzer[1]

[1] *Lawrance Livermore National Laboratory, Livermore, CA, 94550, USA*

[2] *Department of Physics, University of Oxford, Parks Road, Oxford OXI 3PU, UK*

[3] *General Atoms, San Diego, CA, 92121, USA*

[4] *Los Alamos National Laboratory, Los Alamos, NM, 87545, USA*

[5] *CEA/DAM/DIF F-91297 Arpajon, France*

[6] *Sandia National Laboratories, Albuquerque, NM, 87185, USA*

(Dated: 12 December 2012)

Spherically expanding radiative shock waves have been observed from inertial confined implosion experiments at the National Ignition Facility. In these experiments, a spherical capsule filled with a Deuterium-Tritium gas mixture and with a cryogenic Deuterium-Tritium fuel layer is compressed from an initial diameter of 2 mm to a diameter of $\sim$50 μm, with a fuel density > 500 g/cm^3 and a peak pressure of order 100 GB. After peak compression has been reached, the dense shell of assembled fuel and ablator that surrounds the hot central core begins to expand, driving a strong shock outwards into the in falling previously ablated material. Approximately 200 ps after the expansion has begun, x-ray emission from shock heated matter is observed as the shock breaks out of the optically thick dense fuel shell into the lower density ($\sim$1 g/cm^3), optically thinner ablation front. The expansion of the shock heated matter is temporally and spatially resolved and indicates a shock expansion velocity of $\sim$300 km/s. The temporal evolution of the luminosity produced from the shock heated matter was measured at photon energies between 6.1 and 13.87 keV and a peak luminosity of $\sim$3 GW for an implosion driven with 1.66 MJ of laser energy was observed. The observed expansion of the shock and luminosity are consistent with 1-D radiation hydrodynamic simulations. Analytic estimates are in agreement with simulations and indicate that the radiation energy flux modifies the shock front structure leading to the formation of a radiative precursor and a post-shock cooling layer.

In a variety of astrophysical phenomena, including supernova remnants, stellar jets and cataclysmic variable systems, high velocity, radiative shock waves are created. X-ray radiation created from these events offers insight into the composition and physical properties of such systems. In the case of young supernova remnants, the observed spatial variation of x-ray emission has been used to infer the type of stellar progenitor and details of the ejecta distribution and chemical mixing that occurs within the remnant[1]. Additionally the temporal evolution of x-ray emission also offers insight into the hydrodynamic interaction of radiative shock waves with circumstellar medium[2]. Creating strong radiative shocks in the laboratory, where the initial conditions are known and many diagnostics can be used to interrogate the shock evolution and x-ray emission over hydrodynamic time scales not obtainable in a single stellar remnant system, can be used to test hypothesis and inform our understanding of young supernova remnants.

The National Ignition Facility[3] (NIF) is a unique scientific resource, as it has the capability to compress matter to unprecedented densities (1000 g/cc), pressures (100 Gbar), and temperatures (10 keV)[4]. Matter at such extreme states, such as those created in an inertial confined fusion experiment, is of interest for studying a variety of astrophysical phenomena including the radiative hydrodynamics of young supernova.[5]. Laser driven radiative shocks have previously been studied in one dimensional in low density ($\sim$ mg/cc) xenon filled gas tubes, where radiative effects such as the creation of a radiative precursor and a dense collapsed downstream cooling layer have been observed[6–8]. In spherical geometry, the hydrodynamic instabilities of Sedov-Taylor blast waves driven into low density xenon and nitrogen gas filled chambers have been studied using shadography to probe fluctuations in the index of refraction at the shock front[9]. In this work, we present results detailing the creation of a spherically expanding radiative shock wave driven by a dense ($\sim$500 g/cc) shell of ejecta, produced by an inertial confined fusion experiment at the NIF. The temporal evolution of the expansion of the shock and luminosity from the shock heated matter are directly measured and found to be in good agreement with radiation hydrodynamic simulations.

At the NIF, cryogenic thermonuclear implosion experiments are being performed to create an inertial confined fusion reaction using the indirect drive technique[10]. Figure 1 a) shows the experimental setup of an indirect drive implosion experiment. In this method, lasers are used to irradiate the inside wall of a high Z hohlraum, creating an x-ray drive that compresses and confines the fuel capsule to sufficient densities and temperatures to initiate the fusion

reaction. The laser drive is comprised of 192 laser beams, each of which is at a wavelength of 351 nm. As shown in Fig. 1 a), half of the beams are directed into the cylindrical hohlraum through the upper laser entrance hole (LEH), and the other half through the lower LEH. The gold or urainium lined hohlraum converts the laser drive via inverse bremsstrahlung into an x-ray drive with an effective temperature of ~ 300 eV. Experiments have used up to 1.9 MJ of total laser energy and have reached peak powers of 500 TW.

Figure 1 b) details the dimensions and composition of a cryogenic ignition capsule[11]. The capsule has an initial outer diameter of ~ 1 mm and is composed of several layers of plastic (CH) ablator that surround a solid deuterium-tritium (DT) ice layer and is filled with a 50:50 mixture of DT gas. The x-ray drive ablates the outer plastic (CH), creating the pressure which causes the capsule to implode. In current experiments, the capsule converges from an initial radius of $\sim$1 mm to a minimum central DT hot spot radius of $\sim$25 μm. At peak compression, the pressure, temperature, and density of the DT gas rise to approximately 100 Gbar, 2-4 keV, and 100 g/cm^{-3}, respectively. The central hot spot maintains these pressures, densities and temperatures for a duration of $\sim$200 ps.

Two hardened gated x-ray imager (hGXI) diagnostics[12] temporally and spatially resolve the x-ray emission from the compressed core over a $\sim$1 ns duration along the polar and equtorial axes (Fig. 1). Each hGXI uses a pinhole array to image x-rays created via bremsstralung from the hot core onto a four strip gated micro-channel plate (MCP) detector. The gain along each strip of the MCP varies with time, creating a total temporal length along each strip of $\sim$230 to $\sim$180 ps for the polar and equatorial hGXI, respectively. Additionally, the gain of each strip is typically delayed 200 ps from adjacent strips. Thus, images created by the pinhole array at different spatial locations are captured at different times, and a continuous record of the x-ray emission is recorded. Each hGXI has a magnification of 12X, a spatial resolution of $\sim$10 μm, and is filtered with 2575 μm of kapton. The polar and equatorial hGXI has a temporal gain width of 100 and 40 ps, respectively. Figure 1 c) and e) show the x-ray image of the hot DT core at peak x-ray emission taken along the polar and equatorial axes for an implosion experiment that used 1.6 MJ of total laser energy, and a peak laser power of 370 TW (N120412). The burn width of the implosion is defined as the full width half maximum (FWHM) of the integrated signal within the 17% contour of emission vs. time, and for this experiment was found to be 149 $\pm$ 50 ps. To quantify the symmetry of the implosion, a contour, here shown in red, corresponding to 17% of the peak
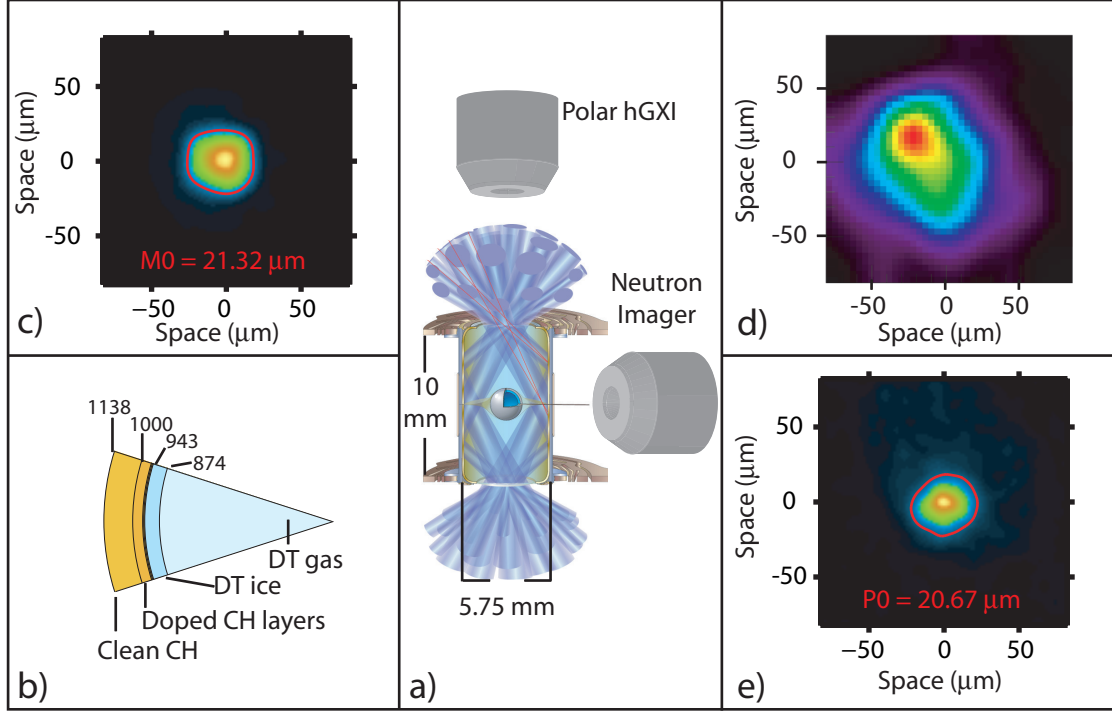
FIG. 1. (Color online) a) Experimental setup, a 10 mm long hohlraum with a top and bottom laser entrance holes of 5.75 mm in diameter, is illuminated using 192 laser beams with a combined energy of up to 1.6 MJ. The resulting hohlraum x-ray drive implodes a cryogenic capsule target, located in the center of the hohlraum. The x-ray self emission from the imploding capsule is imaged along the polar and equatorial (not shown) axis using two harden gated x-ray imager (hGXI) diagnostics. Primary neutrons (14 MeV) created in the hot central core are down scattered in the surrounding dense DT shell. The neutron imager (NI) diagnostic images both the primary and down scattered (6-10 MeV) neutrons along the equatorial axis. b) Details of the initial composition and size of the capsule given in microns. c) An image of the x-ray self emission at peak compression as seen from the polar hGXI diagnostic. The red contour indicates an average radius of 21.32 μm at a value of 17% of peak emission. d) A down scattered image from the NI diagnostic showing the dense shell of DT ice that surrounds the core of the implosion. The down scattered image has a P0=41 μm. e) An image of the x-ray self emission at peak compression as seen from the equatorial hGXI diagnostic. The red contour indicates an average radius of 21.67 μm at a value of 17% of peak emission.

5

x-ray emission, is found and decomposed into Fourier or Legendre modes for the polar and equatorial images, respectively. Surrounding the hot spot is the dense compressed shell of DT fuel and unablated plastic. This shell is at the same pressure of the hot spot, but at a density of $\sim$500-1000 g/cm^{-3} and therefore at a much lower temperature than the hot spot. Consequently, the hGXI diagnostics only observes emission from the lower density hot core while emission from the colder dense shell is not detected. Simulations indicate that the 17% contour of the hot spot emission can be used to infer the inner radial shape of the cold dense DT fuel shell.

The diameter and density of the dense shell surrounding the hot spot is diagnosed by a variety of neutron detectors that can discriminate between primary and down scattered neutrons. Within the hot dense core, deuterium and tritium ions fuse, creating a primary neutron at 14.1 MeV and a 3.5 MeV alpha particle. A fraction of the primary neutrons will lose energy through collisions as they pass through the dense shell of compressed DT fuel and unablated plastic and are called down scattered neutrons. The primary and down scattered neturons are detected by the neutron imager (NI) diagnostic and neutron time of flight detectors (NTOF). Figure 1 d) is an image of the down scattered neutrons with energies between 6 and 10 MeV, and shows the shape of the dense shell that surrounds the hot spot. The 17% contour of the down scattered image has a P0 of 41 μm and is indicative of the outer radius of the dense shell. The density within this shell is inferred from the ratio of down scattered neutrons to primary neutrons detected on the NTOF detectors; for the experiment shown in Fig. 1, the density was found to be $\sim$900 g/cc. The ion temperature of the hot core at stagnation is inferred from the width in energy of the primary neutron spectrum and was found to be 1.84 keV for this experiment. Using the neutron yield, ion temperature, volume of the hot core, and the burn duration, the core pressure is inferred[13] and for this experiment found to be $\sim$150 Gbar.

The pressure within the hot core reaches a maximum as the inward velocity of the fuel shell decelerates and approaches zero. During this time period, the core and surrounding dense shell come into pressure equilibrium. After the implosion has stagnated, the core and dense shell begin to expand outwards as internal energy is transferred back into kinetic energy. A shock is created as the dense shell expands outwards into the much lower density CH plasma that surrounds the implosion. Treating the expansion of the dense shell as a piston, the velocity of the shock can be related to the downstream material (piston) velocity

via the Rankine-Hugoniot (RH) relations as,

$$D = \frac{\left(u_2 - \frac{\rho_1}{\rho_2}u_1\right)}{\left(1 - \frac{\rho_1}{\rho_2}\right)} \tag{1}$$

here, ρ, u, and D are the material density, material velocity, and shock velocity in the laboratory frame, respectively. Subscripts 1 and 2 denote the properties upstream and downstream of the shock front. For $u_2 >> \rho_1 u_1/u_2$, and in the strong shock limit where $\rho_1/\rho_2 = 1/4$ for $\gamma = 5/3$, Eqn. 1 indicates that $D = (4/3)u_2$, where u_2 is equal to the piston velocity of the expanding shell. This velocity is in turn related to the kinetic energy and mass of the expanding shell. It is therefore expected that the shock velocity is related to the amount of energy deposited into the implosion, and not necessary indicative of the peak stagnation pressured reached. Additionally, it is expected that implosions which use similar amounts of laser input energy and laser pulse shape should produce outward going shocks with similar velocities.

As the shock expands, it sweeps up, compresses and heats the surrounding material. Thermal radiation is emitted form the shocked material. This radiation can be spatially and temporally resolved by diagnostics, and can be used to determine the shock front location and shock velocity. The shock velocity is related to the post shock material temperature via RH relations. It can be shown that $T_2 \propto D^2$, where T_2 is the downstream post shock material temperature. As the shock velocity increases, the post shock temperature, and thus radiative energy flux, F, that scales as $F \propto T_2^4$, increases rapidly. If the magnitude of the radiative energy flux is such that it modifies the shock dynamics as described by the RH relations, then the shock can be called a radiative shock. In these experiments, the observed shock velocity and post shock structure, indicate a strongly radiative shock is produced from the expansion of the dense DT and unablated CH shell after stagnation.

Figure 2 shows the temporal evolution of the x-ray emission detected by the polar hGXI diagnostic, with peak x-ray emission from the central core occurring on the first strip of the detector at $t = 0$. On the second strip of the detector, a ring of x-ray emission suddenly appears at t≈200 ps and at a initial radius of 105 μm. This emission is then observed to expands outwards at a velocity of ∼330 km/s over the next 300 ps before the luminosity drops below the detectable level of the instrument. The out going spherical shock, driven by the expanding dense shell, creates a shell of shocked material. The limb brightening of
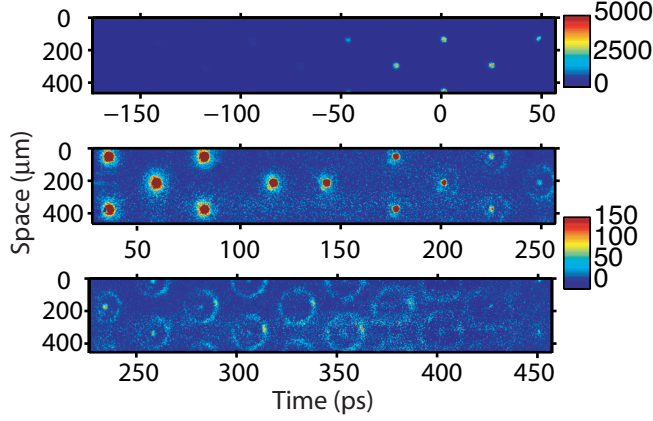
FIG. 2. (Color online) Image from the polar hGXI diagnostic showing the spatial and temporal evolution of the x-ray emission. Time = 0 denotes peak x-ray emission. Approximately 200 ps after peak x-ray emission, a limb brightened shell of x-ray emission, created by a spherically expanding shock wave, suddenly appears at a radius of ~100 μm. This emission is observed to expand outwards until ~500 ps after peak x-ray emission, at which time the signal drops below the detectable level. The color scale has been changed between strip 1 and strips 2 and 3 to enhance the visibility of the shocked material.

the emission from the shell of shocked material creates the observed ring of emission. The sudden appearance of the ring of emission at a radius of ~100 μm is caused by the shock breaking out of a dense region that is completely optically thick to the radiated emission ($r < 100\mu$m) into the less dense, ablation front region ($r > 100\mu$m) that is optically thin to the high energy tail of the radiated spectrum.

Figure 3 shows data from two implosion experiments detailing the temporal evolution of the radius of x-ray emission produced by the expansion of the dense DT and unablated CH shell after stagnation. The shock velocity is found to be ~300 km/s and is consistent with the velocity observed in a 1-D radiation hydrodynamic simulation that used the same laser input energy and reached a similar stagnation pressure. In Fig. 3, the square and triangular data points represent the radius of x-ray emission from the previously described implosion experiment which used 1.66 MJ and another layered implosion experiment which used 1.42 MJ of laser energy, respectively. The velocity of the shock is found by measuring the temporal rate of change of the limb radius, measured at the outward edge of the emission. This is done in order to minimize the uncertainties in the radial location due to the finite
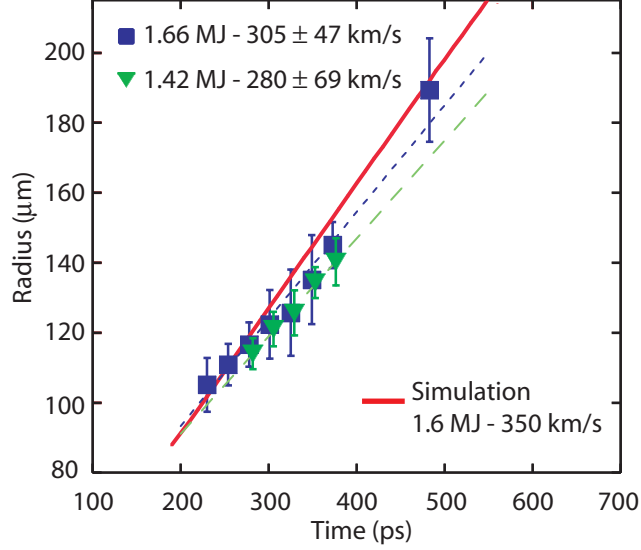
FIG. 3. (Color online) The radius of x-ray emission produced by the outward going spherical shock wave vs. time. Data produced from a DT capsule implosion driven with 1.66 MJ (squares) and 1.42 MJ (triangles) of laser energy is shown. The two dashed lines represent the results from a linear fit to the expansion data. The solid line represents the predicted radius of x-ray emission vs. time from a 1-D HYDRA simulation that used 1.6 MJ of laser energy to drive the implosion.

temporal resolution of the framing camera and from the the limb brightening of the shell of emission. The dashed lines in Fig. 3 represent the best linear fit to the expansion of the shock and indicate a shock velocity of 305 ± 47 km/s and 280 ± 69 km/s for the 1.66 and 1.42 MJ implosion experiment, respectively. The solid line is the radius of emission predicted by the radiation hydrodynamic code HYDRA[14]. Here the simulated results are from a 1-D calculation of an implosion driven with 1.6 MJ of laser energy and which reached a stagnation pressure of ~ 150 Gbar. The simulated emission expands outwards at a velocity of 350 km/s, which is within the 1σ error bar of the measured expansion velocity in the 1.66 MJ implosion experiment. The emission produced by the out going shock is observed up until ~ 500 ps after peak x-ray emission. At this time the emission from the shock drops below the detectable level of the instrument. As no appreciable decrease in shock velocity is seen, the observed decrease in luminosity from the shock heated matter is not due to the dissipation of the strong shock. As will be discussed, simulations indicate that the reduction in luminosity follows a decline in the post shock temperature caused by the decrease of upstream material temperature and velocity.

9

Additionally, the width of the limb indicates that the source of x-ray emission is a narrow shell of emission, with a width $\leq 10~\mu$m. The width (FWHM) of the observed limb is ∼30-35 μm, and has been spatially broadened by the finite temporal response of the detector. Both measurements of the x-ray emission were made using the polar hGXI diagnostic which has a temporal gain width of ∼100 ps. For a shock velocity of ∼ 300 km/s, and a temporal resolution of 100 ps, the ∼30-35 μm limb width indicates a thin region of emitting matter that is equal to or less than the resolution of the diagnostic of ∼10 μm. A thin region of shock heated matter is indicative of a radiative shock, which is consistent with analytic predictions and simulations which will be discussed in more detail later in the paper.

X-ray emission created from the out going shock was also observed in a conversion ablation (ConA) experiment[15] which used the same laser pulse shape and nearly the same laser energy to drive the implosion as the previously discussed 1.66 MJ DT capsule implosion. The expansion velocity of the x-ray emission was measured to be 346 km/s, consistent with the measured expansion velocity in the DT capsule implosion. Figure 4 shows the ConA experimental setup, the measured time resolved radiograph of the capsule implosion and subsequent x-ray emission imaged in one dimension, and a comparison of the measured and simulated radial location for the peak intensity of the expanding x-ray emission. In this ConA experiment, the x-ray drive was produced by 1.62 MJ of laser energy, which is similar to the 1.66 MJ of laser energy used to drive the DT implosion N120412. In addition, the ConA experiment used 48.6 kJ of laser energy to create a Zn He-α x-ray probe to radiograph the capsule during the implosion. The dimensions and composition of the symmetry capsule target (Symcap) that was used are also shown in Fig. 4 a). The Symcap target is nominally the same as the DT layered target, except the DT ice layer has been replaced with an equivalent amount of CH mass and the DT gas fill is replaced with a higher pressure D_2^3He fill that reduces the convergence of the implosion and the neutron yield. The capsule radiograph was imaged in one dimension by a 17 μm wide slit onto a the DISC streak camera that has a temporal resolution of ∼50 ps[16]. An image of the measured radiograph that has been spatially and temporally averaged over 5 μm and 22.5 ps, respectively, is shown in Fig. 4 b). The DISC detector has been filtered with 375 μm of Kapton and 15 μm of zinc. The compressed CH shell creates the two dark limbs that converge inwards with time. Along the center of the spatial axis, a wire fiducial attenuates the x-ray probe and partially obscures the x-ray self emission from the compressed core at times $\pm$500 ps from peak x-ray
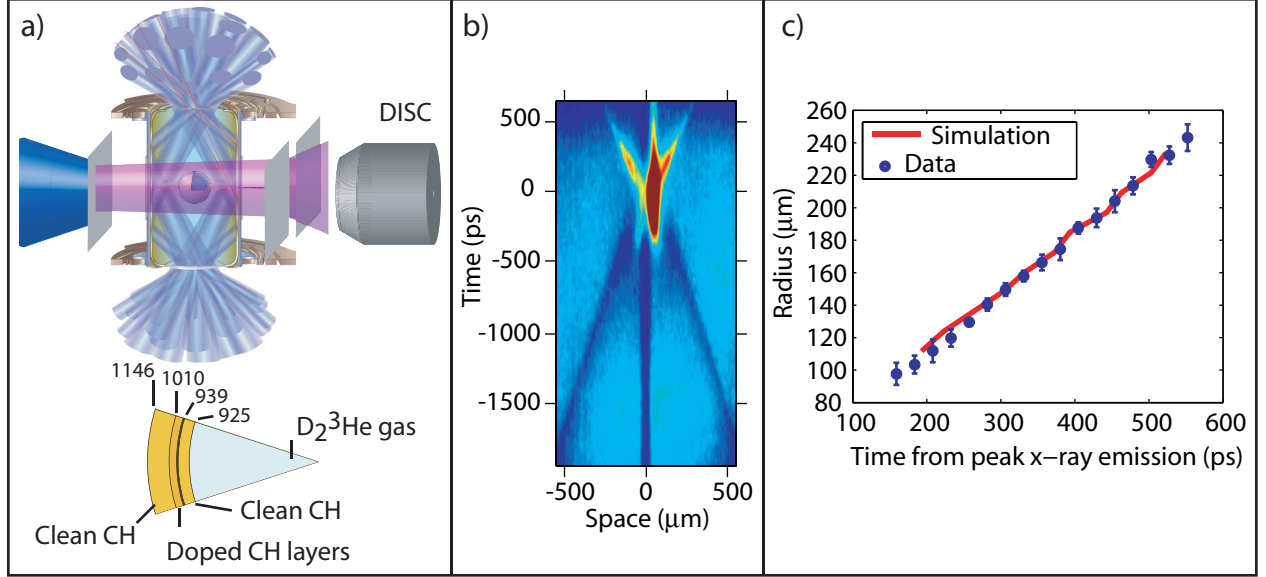
FIG. 4. (Color online) a) Details the convergent ablation experimental setup. Here a probe laser illuminates a zinc foil creating a burst of x-rays that radiographs the capsule over a duration of ~2 ns. A slit images the capsule radiograph in one direction onto the DISC streak camera, which temporally resolves the implosion. The dimensions in microns and composition of the capsule target are also shown. Here a symmetry capsule target is used which replaces the DT fuel layer and gas fill by an equivalent mass of CH and a D_2^3He gas fill, respectively. b) The 1-D radiograph vs. time of a capsule implosion. The dense shell absorbs the x-ray probe creating two dark limbs which converge inwards with time as the shell is compressed by the hohlraum drive. The dark absorption band located approximately at the center of the capsule is created by a wire fiducal and partially obscures the bright self emission from the core. Time = 0 denotes the time of maximum self emission from the capsule core. Emission created by the outward going radiatve shock is seen to appear at t = ~150 ps. c) Radial location of the peak of emission from the outward going shock vs. time. Data shown in blue is in good agreement simulated emission location shown in red.

emission. At t≈150 ps, two limbs of x-ray emission, created from the outward going shock, are observed to emerge and propagate outwards. The observation of two distinct limbs of x-ray emission is consistent with the 1-D imaging of a shell of expanding x-ray emission.

The average radius of the x-ray emission was measured dividing the distance between the maximum intensity of the two limbs by two. Figure 4 c) shows the measured average radius of the emission vs. time and shows that the shock expands at a nearly constant

velocity over the duration of observation. Each data point is the average radius over the 22.5 ps time interval, with the error bars corresponding to the root mean squared deviation from the average radius over the time interval. Additionally, hydrodynamic simulations, in which a forward Abel transformation is performed and convolved with the instrument response functions to generate simulated DISC radiographs, also predicts the x-ray emission generated by the outward going shock after stagnation[17]. The simulated peak x-ray emission radius vs. time is also shown in Fig. 4 c) as the solid line, and is in good agreement with the measurement. The width and intensity of the limb of x-ray emission are determined by the limb brightening of the shell of x-ray emission and by the finite temporal response of the detector. To determine the velocity of the shock, the average temporal rate of change of the radial location of the outward edge (FWHM) of the x-ray limb was measured and found to be 346 ± 7 km/s, which is consistent with the measured expansion velocity of 305 ± 47 km/s from the companion DT implosion.

A radiative shock can be defined as a shock in which either the radiative pressure or radiative energy flux alters the shock dynamics[18]. In these experiments, it is found that a radiative shock is created by the expansion of the dense DT and unablated CH shell. Here the observed shock is determined to exist in a regime in which the radiative pressure is negligible compared to the material pressure, but where the radiative energy flux is larger than the in flowing material energy flux. When this occurs, the shock front structure and propagation can be quite different compared to shocks in which the radiative energy flux is negligible. This can be seen qualitatively by examining the Rankine-Hugoniot relationship for energy conservation in the frame of the shock given by,

$$\rho_2 U_2 \left(e_2 + \frac{1}{2} U_2^2 + \frac{P_2}{\rho_2} \right) + F_2 = \rho_1 U_1 \left(e_1 + \frac{1}{2} U_1^2 + \frac{P_1}{\rho_1} \right) - F_1 \qquad (2)$$

here ρ, P, e, and F are the material density, pressure, internal energy, and radiative energy flux, respectively, where γ is the adiabatic index and the subscripts 1 and 2 denote the upstream and downstream quantities, respectively. In the shock frame, material flows into and out of the shock front at a velocity $U_1 = D - u_1$ and $U_2 = D - u_2$, where D, u_1, and u_2 are the shock velocity, upstream and downstream material velocity in the laboratory frame, respectively. The radiative energy flux is given by $F = \sigma T^4$, where σ is the Stefan-Boltzmann constant and T is the material temperature. Following Zeldovich and Raizer[19],

for systems that are optically thick upstream, $F_1 = 0$ and Eqn. 2 can be rewritten as,

$$\rho_2 U_2 \left(e_2 + \frac{1}{2} U_2^2 + \frac{P_2}{\rho_2} \right) = \frac{\rho_1 U_1^3}{2} - \sigma T_2^4 \qquad (3)$$

where $P_2 >> P_1$, has been assumed. The right hand side of Eqn. 3 depends only on the in flowing material energy flux, given by $\rho_1 U_1^3/2$ and the radiative energy flux. For systems in which $\rho_1 U_1^3/2\sigma T_2^4 \lesssim 1$, the effect of the radiative energy flux on the dynamics of the shock structure and propagation must be considered.

Both the in flowing material and radiative energy flux depend strongly on the shock frame in flowing material velocity U_1. In these experiments, the radiative shock develops as it breaks out into the ablation front of the x-ray drive. Here U_1 is significantly larger than the observed shock velocity D, due to the comparable upstream in flowing material velocity u_1. As the capsule implodes, the x-ray drive continuously ablates material from the CH shell. The ablated material is removed with an outward velocity equal to the isothermal ion sound speed in a partial ionized CH plasma, $c_s = \sqrt{(Z+1)KT_{rad}/M_{avg}} \approx 115$ km/s, for $Z_{avg} = 2.5$, $T_{rad} = 250$ eV, and $M_{avg} \approx 6.5 m_p$, where m_p is the proton mass. In the laboratory frame, the in flowing material velocity is given by, $u_1 = c_s - v_{imp}$, where v_{imp} is the implosion velocity of the CH shell. The previously discussed ConA experiment, which used nearly the same laser drive conditions has measured the peak implosion velocity of the fuel to be 300 km/s, setting the upper limit of $u_1 = -185$ km/s in this experiment. With an observed shock velocity of $\sim$300 km/s an upper limit of $U_1 = 485$ km/s on the in flowing material velocity in the shock frame can be used when calculating the in flowing material energy flux and when estimating the post shock temperature. The in flowing material energy flux also depends on the upstream density, ρ_1. At the ablation front, the upstream density can be estimated to be $\sim$1 g/cc using the relation $\sigma T_{rad}^4 = 4\rho_1 c_s^3$, which describes the balance of energy flux from an ablative heat wave[20]. With $U_1 = 485$ km/s and $\rho_1 = 1$ g/cc, the in flowing material energy flux is found to be 5.7x10^{19} W/m^2.

The radiative flux, F_1, can be estimated by solving for the post shock temperature, T_2 from the RH relationships. Ignoring radiative effects and in the limit of $P_2 >> P_1$, the post shock temperature can be estimated as,

$$T_2 \approx 2 \frac{A}{k_b(Z+1)} \frac{\gamma_2 - 1}{(\gamma_2 + 1)^2} \left(D - u_1 \right)^2 + T_1 \qquad (4)$$

here, k_b is the Boltzmann constant, A is average atomic weight, and Z is the average ionization state. As previously discussed, in this experiment the hohlraum drive heats the ablated

13

upstream in flowing material to a $T_1 \approx 250$ eV. Equation 4 indicates that both the large upstream material velocity, u_1, and temperature, T_1, will significantly increase the post shock temperature compared to a system in which both u_1 and T_1 are negligible. Using a post shock $Z_{avg} = 3.5$, and $\gamma_2 = 5/3$, a shock velocity $D = 300$ km/s, and $u_1 = -185$ km/s, a post shock temperature $T_2 \approx 915$ eV and subsequent radiative flux $F_1 = 7.2 \text{x} 10^{20}$ W/m^2 is estimated. The ratio of material to radiative energy flux in this experiment is then expected to be $\rho_1 U_1^3 / 2 F_1 \approx .08$, which is much less than unity, indicating that the observed shock is radiative.

A finely zoned radiation hydrodynamic simulation of a capsule implosion in 1-D shows the detailed shock evolution, breakout, and rapid rise in the radiance of the shock heated matter that is consistent with experimental observations. In this simulation, the laser drive energy of 1.6 MJ and stagnation pressure of 150 Gbar were matched to the laser drive and inferred stagnation pressure for the experiment discussed above. Figures 5 a), b), and c) show the evolution of the electron temperature, material density, and velocity at times $\Delta t = 0$, 100, and 200 ps from stagnation, respectively. Figure 5 d) shows the radiance of the material, taking into account the detector filtering, at these time intervals. From these simulations it is observed that the outward going shock originates at the outer edge of the dense shell of DT fuel and unablated CH as the shell begins to expand just after stagnation. Figure 5 a) shows this initial state. Here the density profile shows a shell with a peak density of 359 g/cc at a radius of 60 μm. This shell surrounds the lower density central core which at this time has a peak electron temperature of 1.75 keV. The dashed line is the material velocity and indicates that the implosion has reached stagnation as the velocity of the core and dense shell are nearly zero. At radii larger than the radius of the dense shell, a decreasing gradient in the density profile has developed. The velocity of this unablated material is still flowing inwards at a velocity of ~200-250 km/s. At this time, the electron temperature at r=150 μm is equal to the hohlraum drive temperature of 260 eV, and the temperature profile indicates the ablation front is at a radius of ~120 μm. The temperature within the low pressure unablated density gradient is ~50 eV. There is a sharp increase in the electron temperature, with respect to the surrounding material, within the quasi-isobaric high pressure core and dense shell. However, as the material velocity indicates, an outward moving shock has not yet developed.

Figure 5 b), at $\Delta t = 100$ ps from stagnation, shows a shock being driven outwards into
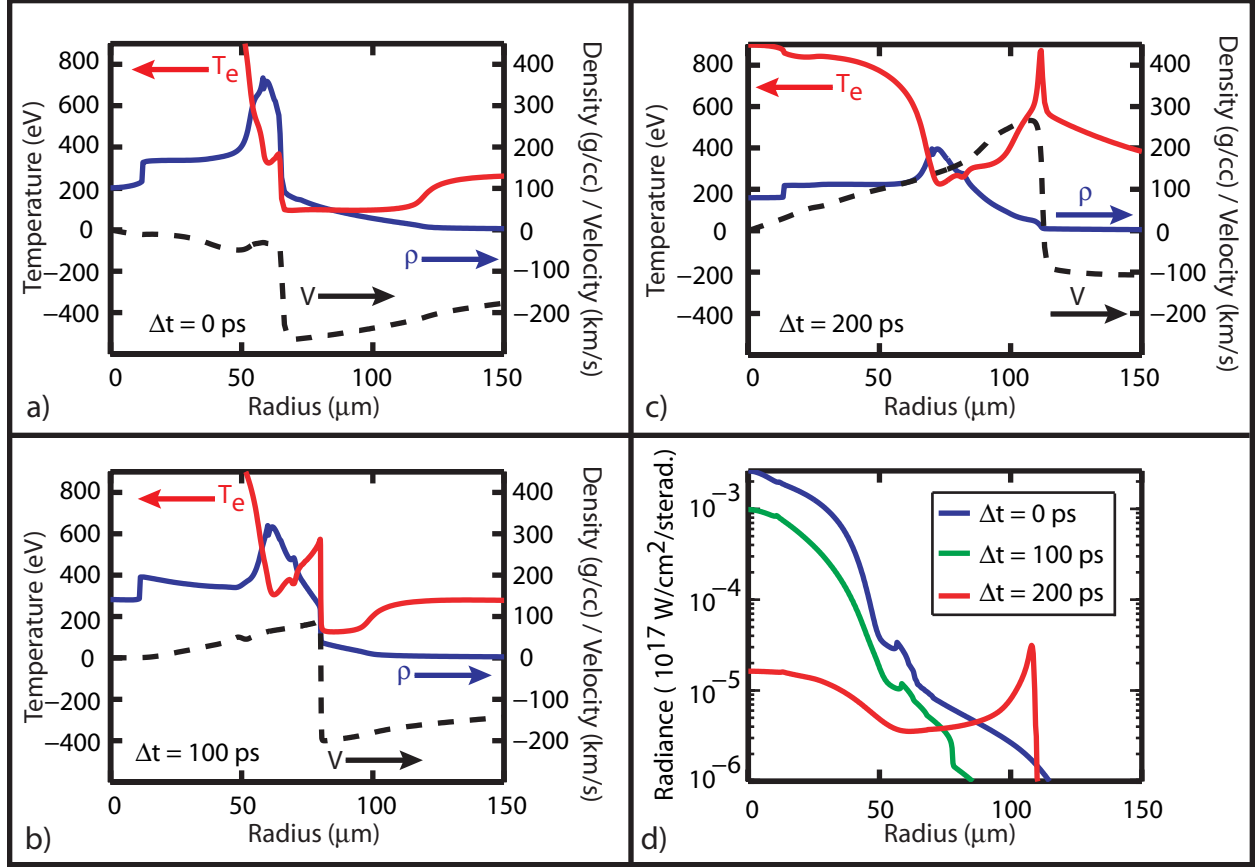
FIG. 5. (Color online) Results from 1-D radiation hydrodynamic simulations showing the evolution of the electron temperature (red), material density (blue), and material velocity (dashed black) profiles at $\Delta t = 0$, 100, and 200 ps from stagnation, in a), b), and c), respectively. A strong shock is driven after stagnation by the expansion of the dense shell of DT fuel and unablated CH into the lower density surrounding CH plasma. d) The simulated radiance of the material, including the detector filter transmission, at $\Delta t = 0$, 100, and 200 ps from stagnation. Simulations are in agreement with experimental observations that show the sudden appearance of a ring of x-ray emission at a radius of ~ 100 μm hundreds of picoseconds after peak x-ray emission.

the surrounding CH ablator. The sharp discontinuity in the electron temperature, density, and material velocity at r=~ 80 μm, with a positive post shock velocity, indicates the shock front location. At this time, the optical depth of the material ahead of the shock front is large enough to absorb all of the outward radiation. This can be seen by examining the radiance of the material at this time step in Fig. 5 d), where the radiance has decreased at r=80 μm between time at stagnation and $\Delta t = 100$ ps. Additionally, the large amount

of optical attenuation can be seen in the electron temperature profile in Fig. 5 b), which shows an extremely sharp discontinuity at r=80 μm, indicating that the radiation from the shocked material is reabsorbed over a very small scale length, and the upstream material (r>80 μm) is largely unaffected and unaware of the shock.

In Fig. 5 c) the shock has now broken out of the higher density optically thick region, into a lower density region where the optical depth has decreased to a level where a sudden increase in the radiance is observed at a radius corresponding to the shock front location at r=108 μm. This sudden increase in radiance approximately 200 ps after stagnation can clearly be seen in Fig. 5 d) and leads to a limb brightened ring of detected emission, consistent with observations from multiple implosion experiments.

In Fig. 5 c), the increase in the electron temperature ahead of the shock front, followed by a sharp spike followed by rapid cooling in temperature just behind the shock front, indicate that radiation transport from the shock heated matter is significantly modifying the shock front structure. This simulation shows that at this time radiation emitted at the shock front travels downstream into a median that is optically thick downstream and travels upstream into a medium that is optically thick to a portion of the emitted spectrum. This type of shock can be called an optically thick radiative shock and is generally described as a shock in which a radiative precursor is created upstream from the shock front, followed by a short optically thin cooling zone just behind the shock front, in which the density further increases as the post shock temperature rapidly cools and approaches the upstream temperature[21].

The amplitude and temporal evolution of the x-ray luminosity emitted from the shock heated matter has been measured and found to be in good agreement with results from radiation hydrodynamic simulations. The temporal evolution of the x-ray luminosity from a stellar supernova is often used to infer information about age and type of progenitor. Observations of such light curves show variations luminosity with time, that have been attributed to variations in the density of the interstellar medium[22]. The ability to create, diagnose, and simulate such x-ray light curves offers an opportunity to study x-ray emission from astrophysical radiative shocks in a scaled laboratory system. Additionally, the spatial variance in limb brightened emission intensity can be used to study hydrodynamic instabilities that can develop during and after the implosion.

The solid squares and triangles in Fig. 6 show the temporal evolution of the luminosity that was measured for the two cryogenic DT implosion experiments previously discussed
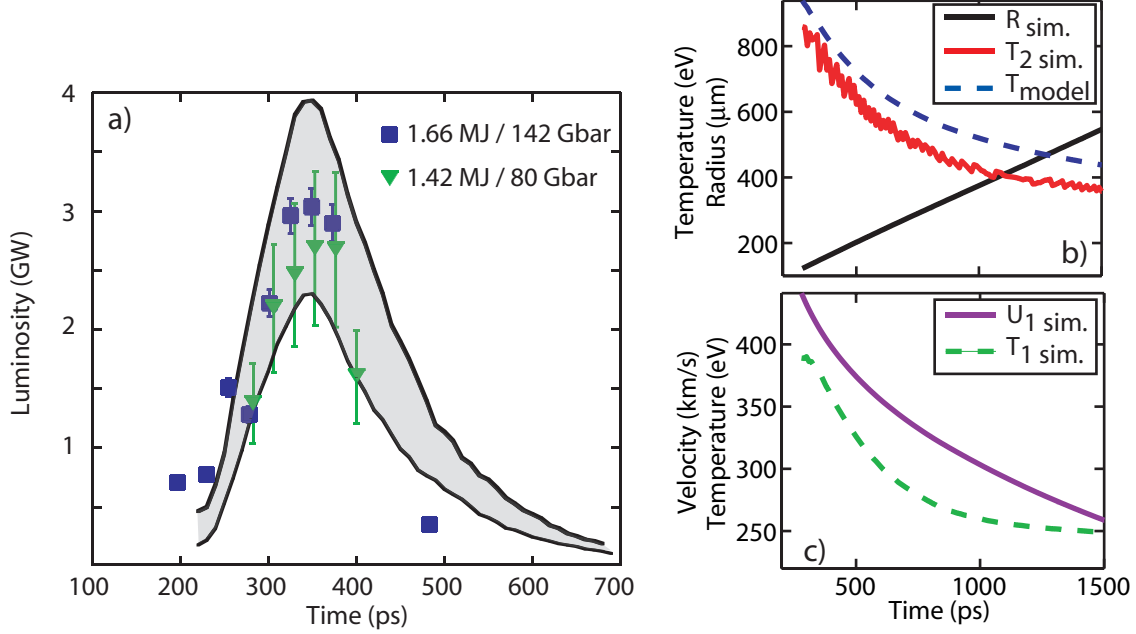
FIG. 6. (Color online) a) Luminosity of the limb brightened ring of x-ray emission vs. time, at x-ray energies between 6.1 and 13.87 keV. The solid squares and triangles are the observed luminosity produced from an implosion driven by 1.66 and 1.42 MJ of laser energy, respectively. The solid lines are the predicted luminosity profiles from 1-D hydrodynamic simulations. The upper curve is from a simulation that drove the implosion with 1.6 MJ of laser energy and the lower curve is from a simulation that used 1.4 MJ of laser energy. b) Results from the 1.6 MJ simulation showing the temporal evolution of the shock front (black), the peak post shock electron temperature (red), and a simple analytic prediction of the post shock temperature (dashed). c) The temporal evolution of the in flowing material velocity, U_1 (solid), and upstream temperature, T_1 (dashed), taken from the 1.6 MJ simulation.

conducted with 1.42 and 1.66 MJ of laser energy, respectively. The solid curves represents the luminosity predicted from HYDRA simulations in which the radiated luminosity was convolved with the temporal instrument response and material filtering to generate predicted x-ray light curves. The upper curve is the predicted result from an implosion driven by 1.6 MJ laser energy, and the lower solid curve is the result from an implosion driven by 1.4 MJ of laser energy. The range of x-ray energies detected is estimated by multiplying the thermal spectrum from the expected peak shock temperature of 1 keV with the spectral response of the 2.5 mm of kapton filtering. It is found that the peak of the spectral transmission occurs

17

at 8.8 keV and that the measurement is sensitive over a spectral range from 6.1 to 13.87 keV, where the spectral range has been defined to be the energy at which 10% of the peak transmission is reached. The observed and simulated maximum luminosity are within 50% of each other and the amplitude of both the measured data and simulated results show a similar temporal evolution.

The luminosity of x-rays observed in these experiments is strongly dependent on the post shock temperature. Here Bremsstrahlung, or free-free emission generated from the forward going shock is the primary source of x-rays. The luminosity over the observed spectral range scales as,

$$L \propto Z^2 n_e n_i T_2^{1/2} V \left[- e^{-\frac{E}{k_b T_2}} \right] \Big|_{E_{min}}^{E_{max}} \tag{5}$$

here, Z is the ionization state, n_e is the electron density, n_i is the ion density, T_2 is the post shock electron temperature, V is the volume of shocked material, E_{min} and E_{max} are the lower and upper spectral energy range of the measurement, respectively. As seen in Fig. 5, a peak luminosity created by the outward going shock from the implosion experiment carried out with 1.6 MJ of laser is larger than the peak luminosity in the experiment conducted with 1.4 MJ of laser energy. An increase to the laser drive energy will increase the outward going shock velocity, leading to an increase in the post shock temperature, T_2. Since our observation is centered at 8.8 keV, which is several times the expected shock temperature, a small change in the post shock temperature will result in a relatively large change in the observed luminosity. For example, over the spectral range from 6.1 to 13.87 keV, for a fixed charge state, density and volume, the luminosity is found to change by $\sim 50\%$ as the T_2 is changed by 10% from 1000 to 900 eV.

In both the measured and simulated x-ray light curves, the luminosity initially increases over the first ~100 ps of observation, reaches a maximum value at ~350 ps from peak x-ray emission and then rapidly decreases by ~5-7X over the next 150 ps. Post processing the luminosity data from the simulations, it was found that the rapid increase in luminosity over the first 100 ps of observation is due to the 100 ps temporal gain width of the detector.

The rapid decline in luminosity within the observed spectral range is determined to be caused by a decrease in the shocked material density and post shock temperature. As the measurement is made over a spectral range that is several times the temperature of the shocked material, the sharp decline in luminosity is mostly due to the decrease of the post shock material temperature. One can estimate the decline in luminosity due to the decrease

in material density by taking the ratio of Eqn. 5 for two different radial locations, and assuming a fixed charge state and temperature. This ratio of initial to final luminosity can then be written as $R = (n_{eo}/n_{ef})^2 V_i/V_f$, where the i and f subscripts denote the inital and final quantities, respectively. The simulated density profile is found to obey a $\rho \propto r^{-1.8}$ dependence. Figure 3 taken with Fig. 6 indicates a luminosity ratio $R \approx$ 5-7 as radius of the shock expands 130 μm to 180 μm for the 1.6 MJ implosion experiment. The simulations indicate the width of the shock changes only slightly with time, so taking the width as approximately constant, $V_i/V_f \approx r_i^2/r_f^2$ where r is the radius of the shock. With these conditions, the expected ratio of luminosity between 130 to 180 μm for a fixed post shock temperature is ~ 1.7, much less than the observed or simulated ratio. This estimate isolates the effect of decreasing density on the luminosity by assuming a fixed post shock temperature. However as shown in Fig. 6 b), the post shock electron temperature is not constant, but rather is observed to decline with time.

Observations and simulations of the temporal evolution of the shock front radius, shown in Fig. 3, and Fig. 6 b), respectively, show that the shock velocity is approximately constant, indicating that the decline in post shock temperature is not due to the deceleration of the shock. Examining Eqn. 4, it is found that the post shock temperature can decrease, for a constant shock velocity D, if either the upstream material velocity, u_1, or upstream temperature, T_1, decrease. Figure 6 c) shows that the simulated in flowing material velocity $U_1 = D - u_1$, and T_1 are both decreasing with time. As the shock propagates outwards in time to larger radii the material density and optical depth both decrease. As the upstream material becomes optically thin to the radiation from the post shock material, the temperature of the upstream precursor drops and approaches the hohlraum drive temperature. Additionally, the decrease in U_1 with time is a result of the smaller u_1 at larger radii. At later times, and larger radii, the ablated material that the shock interacts with was generated at earlier times in the capsule implosion, where the the relative difference between $|c_s - V_{imp}|$ is smaller. Using the simulated values for U_1, and T_1 the post shock temperature T_2 was estimated using Eqn. 4 and is shown as the dashed curve in Fig. 6 b). The analytic estimate of T_2 slightly overestimates the simulated value, but has a very similar temporal dependence, indicating the important role played by the upstream temperature and in flowing material velocity on the post shock temperature and subsequently on the luminosity from the shock heated matter. In simulations the post shock temperature is found to decrease from an

initial temperature $T_i = 820$ eV to a final temperature $T_f = 695$ eV from a radius of 130 to 180 μm. To estimate the effect of the decline in temperature on the luminosity, the ratio of initial to final luminosity $(T_i^{1/2}/T_f^{1/2})\left(e^{6.1/T_i} - e^{13.7/T_i}\right)/\left(e^{6.1/T_f} - e^{13.7/T_f}\right)$ is taken and is found equal to ~ 4, indicating a 4X decline in luminosity due to the decreasing temperature. This decline taken together with the expected decline of 1.6X due to the decrease in density, predicts an overal decline of 6.6X in luminosity from 130 to 180 μm, similar to the decrease observed in both the measurement and simulation.

In conclusion, indirect drive inertial confinement fusion implosion experiments at the National Ignition Facility have produced a spherically expanding radiative shock wave in the laboratory. The radiative shock is produced as the dense shell of assembled fuel and ablator material expands outwards after stagnation, into the hot, ~ 250 eV, dense, ~ 1 g/cc, ablation front plasma which is still converging inwards at a velocity of ~ 150 km/s. Radiation from shock heated matter is observed to appear suddenly $\sim$200 ps after peak x-ray emission as the shock breaks out into the optically thinner ablation front. The expansion of the shock heated matter indicates that the velocity of this shock is $\sim$300 km/s. Analytic estimates show that in these experiments, the high velocity of the observed shock creates a radiative energy flux from the shock heated matter that is greater than the in flowing material energy flux. One dimensional radiation hydrodynamic simulations show general agreement with the observed shock expansion and velocity. The simulations also predict the formation of a radiative shock wave, and shows a radiative precursor upstream of the shock front, a rise in temperature at the shock front, followed by a rapid decline temperature as the post shock temperature approaches the upstream precursor temperature. Additionally, the absolute x-ray luminosity between 6.1 and 13.87 keV, from the shock heated matter was measured and found to be in agreement with the luminosity predicted from radiation hydrodynamic simulations. For the experiment which used 1.6 MJ of laser energy to drive the implosion, the luminosity was observed to decrease from a peak of 3 GW to .35 GW in ~ 100 ps. The decline in the x-ray luminosity is partially due to the decrease in the post shock material density that occurs as the shock propagates outward and primarily due to the decrease in post shock temperature that occurs as the in flowing material velocity and temperature are reduced at larger radii. In the future, by modifying the capsule composition and dimensions, as well as by changing the laser drive conditions, the shock velocity and radiative properties could be tailored to study various regimes related to supernova remnants.

ACKNOWLEDGMENTS

REFERENCES

[1] L. A. Lopez, E. Ramirez-Ruiz, D. Huppenkothen, C. Badens, and D. A. Pooley, ApJ **732**, 114 (2011).

[2] S. Park, D. N. Burrows, G. P. Garmire, J. A. Nousek, R. McCray, E. Michael, and S. Zhekov, ApJ **567**, 314 (2002).

[3] E. I. Moses and C. R. Wuest, Fusion Science Tech **47**, 314 (2005).

[4] NNSA and U. O. of Science, "Basic research directions for user science at the national ignition facility," (2011).

[5] B. Remington, "Preparing for the x games of science," (2007).

[6] A. B. Reighard, R. P. Drake, K. K. Dannenberg, D. J. Kremer, M. Grosskopf, E. C. Harding, D. R. Leibrandt, S. G. Glendinning, T. S. Perry, B. A. Remington, J. Greenough, J. Knauer, T. Boehly, S. Bouquet, L. Boireau, M. Koenig, and T. Vinci, Phys. Plasmas **13**, 082901 (2006).

[7] J. C. Bozier, G. Thiell, J. P. L. Breton, S. Azra, M. Decroisette, and D. Schirmann, Phys. Rev. Lett. **57**, 11 (1986).

[8] S. Bouquet, C. Stéhlé, M. Koenig, J.-P. Chièze, A. Benuzzi-Mounaix, D. Batani, S. Leygnac, X. Fleury, H. Merdji, C. Michaut, F. Thais, N. Grandjouan, T. Hall, E. Henry, V. Malka, and J.-P. J. Lafon, Phys. Rev. Lett. **92**, 225001 (2004).

[9] J. Grun, J. Stamper, C. Manka, J. Resnic, R. Burris, J. Crawford, and B. H. Ripin, Phys. Rev. Lett. **66**, 21 (1991).

[10] J. D. Lindl, P. Amendt, R. L. Berger, S. G. Glendinning, S. H. Glenzer, S. W. Haan, R. L. Kauffman, O. L. Landen, and L. J. Suter, Phys. Plasmas **11**, 339 (2004).

[11] S. W. Haan, J. D. Lindl, D. A. Callahan, D. S. Clark, J. D. Salmonson, B. A. Hammel, L. J. Atherton, R. C. Cook, M. J. Edwards, S. Glenzer, A. V. Hamza, S. P. Hatchett, M. C. Herrmann, D. E. Hinkel, D. D. Ho, H. Huang, O. S. Jones, J. Kline, G. Kyrala, O. L. Landen, B. J. MacGowan, M. M. Marinak, D. D. Meyerhofer, J. L. Milovich, K. A.

Moreno, E. I. Moses, D. H. Munro, A. Nikroo, R. E. Olson, K. Peterson, S. M. Pollaine, J. E. Ralph, H. F. Robey, B. K. Spears, P. T. Springer, L. J. Suter, C. A. Thomas, R. P. Town, R. Vesey, S. V. Weber, H. L. Wilkens, and D. C. Wilson, Phys. Plasmas **18**, 051001 (2011).

[12]S. Glenn, J. Koch, D. K. Bradley, N. Izumi, P. Bell, J. Holder, G. Stone, R. Prasad, A. MacKinnon, P. Springer, O. L. Landen, and G. Kyrala, Rev. Sci. Instrum. **81**, 10E539 (2010).

[13]S. H. Glenzer, D. A. Callahan, A. J. MacKinnon, J. L. Kline, G. Grim, E. T. Alger, R. L. Berger, L. A. Bernstein, R. Betti, D. L. Bleuel, T. R. Boehly, D. K. Bradley, S. C. Burkhart, R. Burr, J. A. Caggiano, C. Castro, D. T. Casey, C. Choate, D. S. Clark, P. Celliers, C. J. Cerjan, G. W. Collins, E. L. Dewald, P. DiNicola, J. M. DiNicola, L. Divol, S. Dixit, T. Doppner, R. Dylla-Spears, E. Dzenitis, M. Eckart, G. Erbert, D. Farley, J. Fair, D. Fittinghoff, M. Frank, L. J. A. Frenje, S. Friedrich, D. T. Casey, M. G. Johnson, C. Gibson, E. Giraldez, V. Glebov, S. Glenn, N. Guler, S. W. Haan, B. J. Haid, B. A. Hammel, A. V. Hamza, C. A. Haynam, G. M. Heestand, M. Hermann, H. W. Hermann, D. G. Hicks, D. E. Hinkel, J. P. Holder, D. M. Holunda, J. B. Horner, W. W. Hsing, H. Huang, N. Izumi, M. Jackson, O. S. Jones, D. H. Kalantar, R. Kauffman, J. D. Kilkenny, R. K. Kirkwood, J. Klingmann, T. Kohut, J. P. Knauer, J. A. Koch, B. Kozioziemki, G. A. Kyrala, A. L. Kritcher, J. Kroll, K. L. Fortune, L. Lagin, O. L. Landen, D. W. Larson, D. LaTray, R. J. Leeper, S. L. Pape, J. D. Lindl, R. Lowe-Webb, T. Ma, J. McNaney, A. G. MacPhee, T. N. Malsbury, E. Mapoles, C. D. Marshall, N. B. Meezan, F. Merrill, P. Michel, J. D. Moody, A. S. Moore, M. Moran, K. A. Moreno, D. H. Munro, B. R. Nathan, A. Nikroo, R. E. Olson, C. D. Orth, A. E. Pak, P. K. Patel, T. Parham, R. Petrasso, J. E. Ralph, H. Rinderknecht, S. P. Regan, H. F. Robey, J. S. Ross, M. D. Rosen, R. Sacks, J. D. Salmonson, R. Saunders, J. Sater, C. Sangster, M. B. Schneider, F. H. Seguin, M. J. Shaw, B. K. Spears, P. T. Springer, W. Stoeffl, L. J. Suter, C. A. Thomas, R. Tommasini, R. P. J. Town, C. Walters, S. Weaver, S. V. Weber, P. J. Wegner, P. K. Whitman, K. Widmann, C. C. Widmayer, C. H. Wilde, D. C. Wilson, B. V. Wonterghem, B. J. MacGowan, L. J. Atherton, M. J. Edwards, and E. I. Moses, Phys. Plasmas **19**, 056318 (2012).

[14]M. M. Marinak, G. D. Kerbel, N. A. Gentile, O. Jones, D. Munro, S. Pollaine, T. R. Dittrich, and S. W. Haan, Phys. Plasmas **8**, 2275 (2001).

[15]D. G. Hicks, B. K. Spears, D. G. Braun, R. E. Olson, C. M. Sorce, P. M. Celliers, G. W.

Collins, and O. L. Landen, Phys. Plasmas **17**, 102703 (2010).

[16]Y. P. Opachich, N. Palmer, D. Homoelle, B. Hatch, P. Bell, D. Bradley, D. Kalantar, D. Browning, J. Zuegel, and O. Landen, Rev. Sci. Instrum. **83**, 10E123 (2012).

[17]R. E. Olson, D. G. Hicks, N. B. Meezan, J. A. Koch, and O. L. Landen, Rev. Sci. Instrum. **83**, 10D310 (2012).

[18]R. P. Drake, *High-Energy-Density Physics: Fundamentals, Inertial Fusion, and Experimental Astrophyiscs* (Springer, Berlin, 2006).

[19]Y. B. Zel'dovich and Y. P. Raizer, *Physics of Shock Waves and High Temperature Hydrodynamic Phenomena* (Dover, Mineola, New York, 2002).

[20]S. Atzeni and J. M. ter Vehn, *The Physics of Inertial Fusion: Beam Plasma Interaction, Hydrodynamics, Hot Dense Matter* (Oxford University Press, USA, 2009).

[21]R. P. Drake, Phys. Plasmas **14**, 043301 (2007).

[22]V. V. Dwarkadas and J. Gruszko, Monthly Notices of the Royal Astronomical Society **419**, 1515 (2012).